Nano Research

Open Access

Research Article

Simultaneous improving luminescence intensity and stability, reduce cation vacancies of rare-earth doped CaF_2 by charge self-compensation

Yuxin Liu, Zhangong Bai, Ao Xu, and Guofeng Wang ✉

Key Laboratory of Functional Inorganic Material Chemistry, Ministry of Education, School of Chemistry and Materials Science, Heilongjiang University, Harbin 150080, China

Cite this article: *Nano Research*, **2026**, *19*, 94908410. https://doi.org/10.26599/NR.2026.94908410

ABSTRACT: Although upconversion rare-earth (RE) materials have excellent luminescence properties, the luminescence intensity and thermal stability of phosphors are not favorable due to RE doping induced vacancies. This work focused on enhancing luminescence intensity and stability of phosphor by charge compensation and three-dimensional (3D) printing. The luminescence results showed that $Ca_{0.697}Yb_{0.2}Er_{0.0015}Tm_{0.0005}F_2$ with charge compensation exhibited luminescence intensity 3.2 times higher than that of $Ca_{0.798}Yb_{0.2}Er_{0.0015}Tm_{0.0005}F_2$ non-charge compensation. The luminescence of resin-coated luminescent materials is still stable after 6 months. The constructed white light-emitting diodes (WLEDs) also exhibit consistent and outstanding color rendering characteristics, with a color rendering index (CRI) of up to 81 and a low color temperature (CCT).

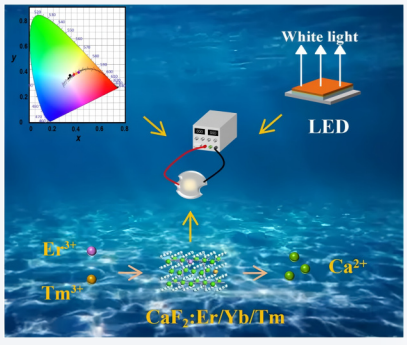

KEYWORDS: upconversion luminescence enhancement, charge compensation, luminescence stability, three-dimensional (3D) printing, density functional theory (DFT)

1 Introduction

The white light-emitting diodes (WLEDs) have the advantages of high efficiency, high brightness, low power consumption, simple structure, low cost, etc. The development of WLEDs utilizing inorganic phosphors as color converters is poised to transform the lighting and display industries. This solid-state lighting approach offers substantial advantages over conventional technologies, including enhanced luminous efficacy, superior stability, and tunable photometric properties [1–4]. At present, WLEDs commonly utilize blue light-emitting diode (LED) chips in combination with yellow phosphors. Nevertheless, the production of blue LED poses a significant challenge. In recent years, researchers have explored near-ultraviolet (NUV) chip-excited red, green, and blue trichromatic phosphors to achieve superior performance in WLEDs [5].

Trivalent RE ions are pivotal due to their distinctive 4f-electron configurations and rich energy levels, enabling luminescence across a broad spectrum from UV to near-infrared (NIR) [6–8]. RE luminescent materials have attracted great attention due to their interesting optical properties such as large stokes shifts, long excited state lifetimes, high quantum efficiencies, stable physicochemical properties, broad emission spectral ranges, and high color purity. A key feature is that their luminescence profiles can be precisely engineered through composition and structural design [9–15]. Consequently, RE materials are increasingly used in a wide range of applications, spanning from traditional lighting and displays to emerging fields like sensing and optical information storage [16, 17]. Furthermore, upconversion (UC) RE materials have been extensively investigated for photon management in diverse applications, including biomedicine, solar energy conversion, sensing, and photocatalysis [18–20]. Among them, fluoride crystals have lower phonon energies than oxide crystals and are known to be excellent matrix materials for lanthanide ions.

In fluoride, the first laser demonstration in 1967 using CaF_2:Er single crystals drew significant attention from researchers [21]. In addition, CaF_2 is an ideal luminescent substrate material with a typical fluorite structure capable of realizing high doping concentrations of foreign ions with low phonon energies, high doping concentrations, and strong stability, and thus can be used as a high-efficiency UC luminescent material [22]. However, when trivalent RE ions replace divalent cations (Ca^{2+}), they can lead to an excess of positive charge, resulting in cation vacancies. These

Received: December 2, 2025; **Revised:** December 31, 2025
Accepted: January 5, 2026

✉Address correspondence to wangguofeng@hlju.edu.cn

vacancies can reduce the luminescence intensity and stability of the sample. To solve this problem, charge compensation can be achieved by adjusting the doping ratio. Specifically, reducing the Ca^{2+} concentration can suppress the substitution of Ca^{2+} by trivalent cations, thereby effectively reducing the number of vacancies in the lattice [23]. 3D printing has emerged as a transformative technology with broad application prospects in fields including healthcare and education, due to cost reductions and commercial availability. Despite the significant advancements in various luminescent materials, such as near-infrared emitting metal halides, highly efficient perovskite emitters, and molecular-based luminophores [24–30], the application of 3D printing in processing them remains relatively unexplored. Conventional methods for creating luminescent components typically involve blending luminescent materials with polydimethylsilo-xane polymers, followed by coating them as thin films on substrates or forming them into shells around ZrO_2 cores. However, these techniques are limited in their ability to fabricate complex architectures and often fail to ensure persistent luminescent performance.

In this work, a series of CaF_2:Yb^{3+}/Er^{3+}, CaF_2:Yb^{3+}/Tm^{3+}, and CaF_2:Yb^{3+}/Er^{3+}/Tm^{3+} were synthesized via a hydrothermal method. These phosphors exhibit tunable panchromatic luminescence along with high thermal and photostability. The structures of CaF_2 and CaF_2:Yb^{3+}/Tm^{3+} were calculated and optimized using density functional theory (DFT). The experimental results show that charge compensation significantly enhances the luminescent intensity of the phosphors. Furthermore, high-quality WLEDs were fabricated using the CaF_2:Yb^{3+}/Er^{3+}/Tm^{3+} phosphor with charge compensation, achieving a high CRI of 81 and a low CCT of 4270 K. By encapsulating these phosphors into photosensitive resins via 3D printing technology, devices with stable luminescence were realized. Thus, owing to its tunable panchromatic emission, CaF_2:Yb^{3+}/Er^{3+}/Tm^{3+} emerges as a highly promising luminescent material for advanced WLEDs.

2 Results and discussion

2.1 DFT calculation and discussion

To begin, we utilize DFT calculations to examine the optimized crystal structure, band structure, density of states (DOS), and partial density of states (PDOS). The optimized structures of CaF_2, Ca_4F_8, $CaYb_2F_8$, and $CaTmYbF_8$ are shown in Fig. S1 in the Electronic Supplementary Material (ESM), with calculated band gap values of 7.598, 6.786, 5.082, and 3.406 eV, respectively. This indirect bandgap of CaF_2 is 7.598 eV, which agrees well with the theoretical result 7.33 eV of Yun et al [31]. DFT calculations indicate that doping CaF_2 with Yb^{3+}/Tm^{3+} reduces its band gap, thereby promoting carrier excitation. Therefore, the ratio of Ca/Yb/Tm can influence the crystal structure and optimize the luminescence properties. The calculated DOS and PDOS for CaF_2 in Figs. S1 and S2 in the ESM reveal that the valence band from −36.55 to −34.65 eV is attributed to the 4s orbitals of Ca atoms, while the band from −5.19 to 0.50 eV is attributed to the 2p orbitals of F atoms. The prominent peak within the range of −25.10 to −14.94 eV comprises contributions from F 2s and Ca 3p orbitals. Additionally, the strong peak in the conduction band (ranging from 7.67 to 14.58 eV) primarily arises from the 3d orbitals of Ca atoms. Upon Yb and Tm doping, a new peak emerges at the top of the valence band, as a result of the 4f orbitals of Yb and Tm atoms, as indicated in Figs. S1 and S2 in the ESM. The findings from the DOS and PDOS analyses highlight the significant role of p orbitals in the valence band, and the joint influence of p and d orbitals in the conduction band.

To further investigate the thermodynamic properties of CaF_2, we calculated the enthalpy, free energy, zero-point energy, entropy (T*S), heat capacity, and Debye temperature for CaF_2, Ca_4F_8, and $CaYb_2F_8$ (Figs. 1(a)–1(i)). Figure 1 shows that both entropy and enthalpy increase with temperature, whereas the free energy decreases. The zero-point energies of CaF_2, Ca_4F_8, and $CaYb_2F_8$ are 0.12, 0.65, and 0.45 eV, respectively. These values suggest enhanced stability for all three compounds at low to moderate temperatures. Analysis of the heat capacity curves in Figs. 1(d)–1(f) shows that the heat capacity rises rapidly at low temperatures before saturating, which is consistent with the Debye T^3 law. The temperature dependence of the heat capacity arises from the specific atomic vibrational modes at intermediate temperatures. Moreover, it is observed that the heat capacity of CaF_2, Ca_4F_8, and $CaYb_2F_8$ approaches Dulong–Petit limit as temperatures nears 1000 K. Figure 1 shows that the heat capacity increases with temperature below 600 K, which can be attributed to the anharmonic effects accounted for in the Debye model. This deviation from the T^3 law at low temperatures is due to an enhanced contribution from low-frequency vibrational modes. Figures 1(g)–1(i) shows the Debye temperature rises sharply at low temperatures. As the temperature continues to rise, the rate of growth gradually decelerates and eventually stabilizes in the high-temperature regime. At high temperatures, the Debye temperature asymptotically approaches a constant value.

Figures 1(j)–1(o) shows the phonon dispersion curves and density of phonon states of CaF_2, Ca_4F_8, and $CaYb_2F_8$. The phonon band gaps spans from −20.0 to 30.0 THz for Ca_4F_8 and from −10.0 to 15.0 THz for $CaYb_2F_8$. These values are higher than those of CaF_2, suggesting stronger bonding interactions in Ca_4F_8 and $CaYb_2F_8$, which contribute to their enhanced stability. The electron wavefunction originates at the valence band maximum, traverses the high-symmetry path G-F-Q-Z-G, and enters the conduction band minimum. The heavy-atom effect of Yb^{3+} shifts the phonon dispersion curve downward (Fig. 1(l)), suppressing high-frequency modes while amplifying low-frequency contributions. Correspondingly, the phonon density of states (Fig. 1(m)) is characterized by pronounced high-frequency peaks, which are attributed to the stretching vibrations of Ca–F bonds.

The phonon density of states (Fig. 1(o)) exhibits a dense low-frequency peak, attributed to localized Yb^{3+} vibrations. Concurrently, the intensity weakens in the high-frequency region, reflecting the modulation effect of RE ions on lattice vibration. It is evident that the incorporation of Yb^{3+} significantly enhances the stability of the dynamics.

The aforementioned DFT calculations demonstrate that Yb/Tm doping effectively modulates the bandgap structure and phonon vibration modes of the CaF_2 system, and enhances stability. This provides a theoretical basis for experimentally designing luminescent materials with high doping concentrations while maintaining structural integrity. Building on this, we systematically adjusted the stoichiometric ratio of Ca^{2+} to RE ions in subsequent experiments. By employing charge compensation strategies to mitigate lattice vacancies caused by valence mismatch, we optimized the luminescent performance.

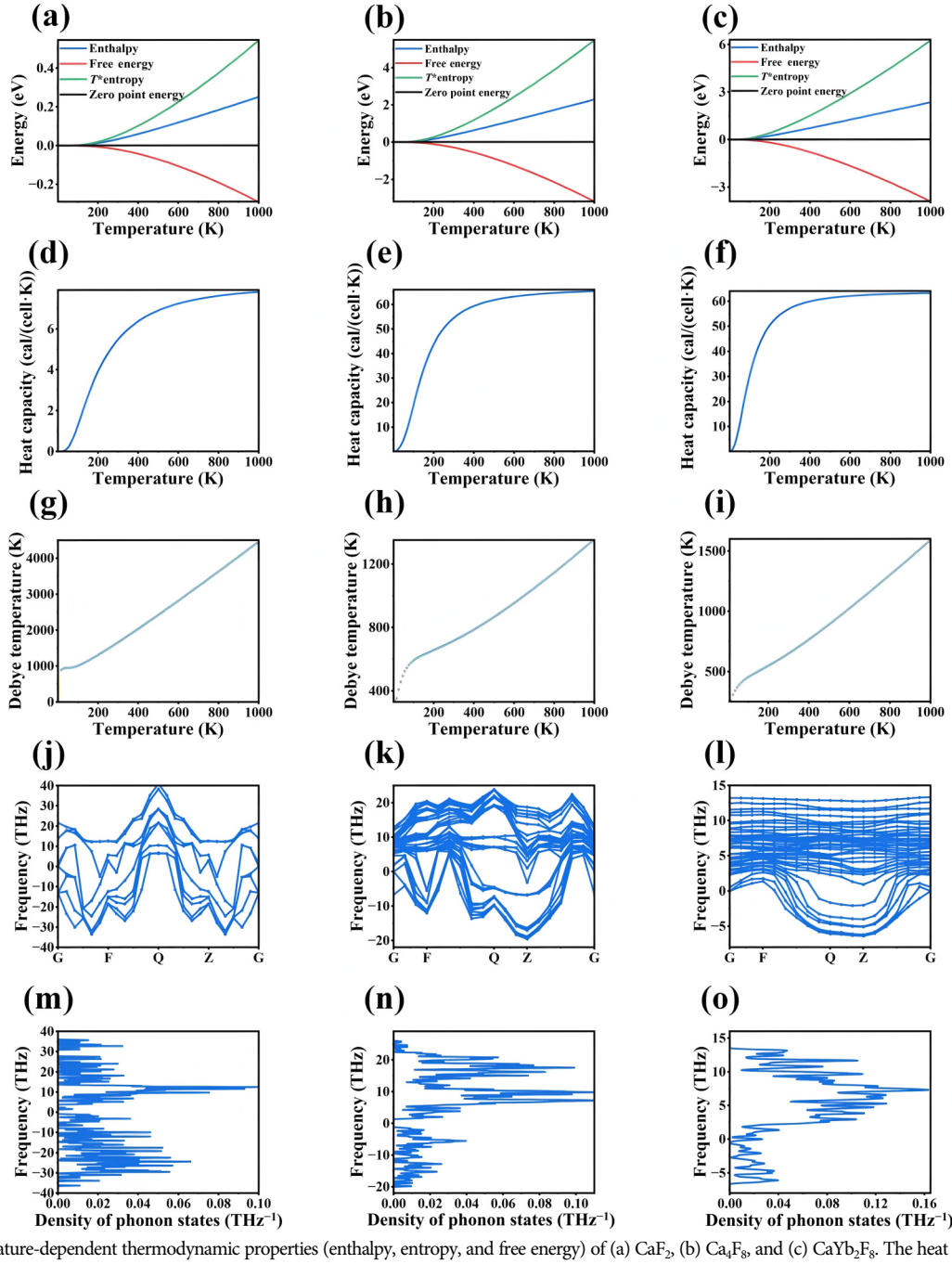

Figure 1 Temperature-dependent thermodynamic properties (enthalpy, entropy, and free energy) of (a) CaF_2, (b) Ca_4F_8, and (c) $CaYb_2F_8$. The heat capacity of (d) CaF_2, (e) Ca_4F_8, and (f) $CaYb_2F_8$. The debye temperature of (g) CaF_2, (h) Ca_4F_8, and (i) $CaYb_2F_8$. The phonon dispersion of (j) CaF_2, (k) Ca_4F_8, and (l) $CaYb_2F_8$. The phonon density of states of (m) CaF_2, (n) Ca_4F_8, and (o) $CaYb_2F_8$.

2.2 Structural characterizations

The process and conditions for synthesizing the material, sample identifiers, experimental methods, and the colorimetric coordinates as defined by the Commission Internationale d'Eléclairage (CIE) can be found in Fig. 2(a) and Tables S1–S6 in the ESM.

The X-ray diffraction (XRD) patterns in Fig. S5 in the ESM indicate that calcium fluoride belongs to the cubic crystal phase. The observed XRD patterns match well with the reference pattern for cubic CaF_2 (JCPDS No. 77-2096). The XRD patterns were also expanded in the range of 26°–32°, as illustrated in Fig. S5(b) in the ESM, where the diffraction angle shows a slight shift to higher degrees of diffraction due to the substitution of larger Ca^{2+} (1.00 Å) ions with smaller ionic radius Er^{3+} (0.88 Å) and Tm^{3+} (0.87 Å) ions. CaF_2 is doped with excess Er^{3+}, Yb^{3+}, and Tm^{3+} ions, so that the Er^{3+}, Yb^{3+}, and Tm^{3+} ions react with NaF to produce $NaErF_4$ (JCPDS No. 27-0689), $NaTmF_4$ (JCPDS No. 27-0814), and $NaYbF_4$ (JCPDS No. 27-1427), which indicates that the Er^{3+}, Yb^{3+}, and Tm^{3+} ions have been successfully doped. Figure S5 in the ESM shows that charge compensation does not fundamentally alter the cubic CaF_2 crystal phase.

Figure 2 and Fig. S3 in the ESM show transmission electron microscopy (TEM) images and high-resolution TEM (HRTEM) images of the synthesized $Ca_{0.78}Yb_{0.2}Er_{0.02}F_2$, $Ca_{0.67}Yb_{0.2}Er_{0.02}F_2$, and

$Ca_{0.697}Yb_{0.2}Er_{0.0015}Tm_{0.0005}F_2$ [32]. TEM images show that CaF_2 nanocrystals are dispersed and uniformly distributed with a diameter of about 10 nm. HRTEM images of single nanoparticles show lattice spacings of approximately 0.320, 0.317, and 0.313 nm for $Ca_{0.78}Yb_{0.2}Er_{0.02}F_2$, $Ca_{0.67}Yb_{0.2}Er_{0.02}F_2$, and $Ca_{0.697}Yb_{0.2}Er_{0.0015}Tm_{0.0005}F_2$, respectively. All of these values correspond to the distance of the (111) planes in cubic CaF_2 (Fig. 2). Charge compensation reduces the (111) spacing from 0.320 to

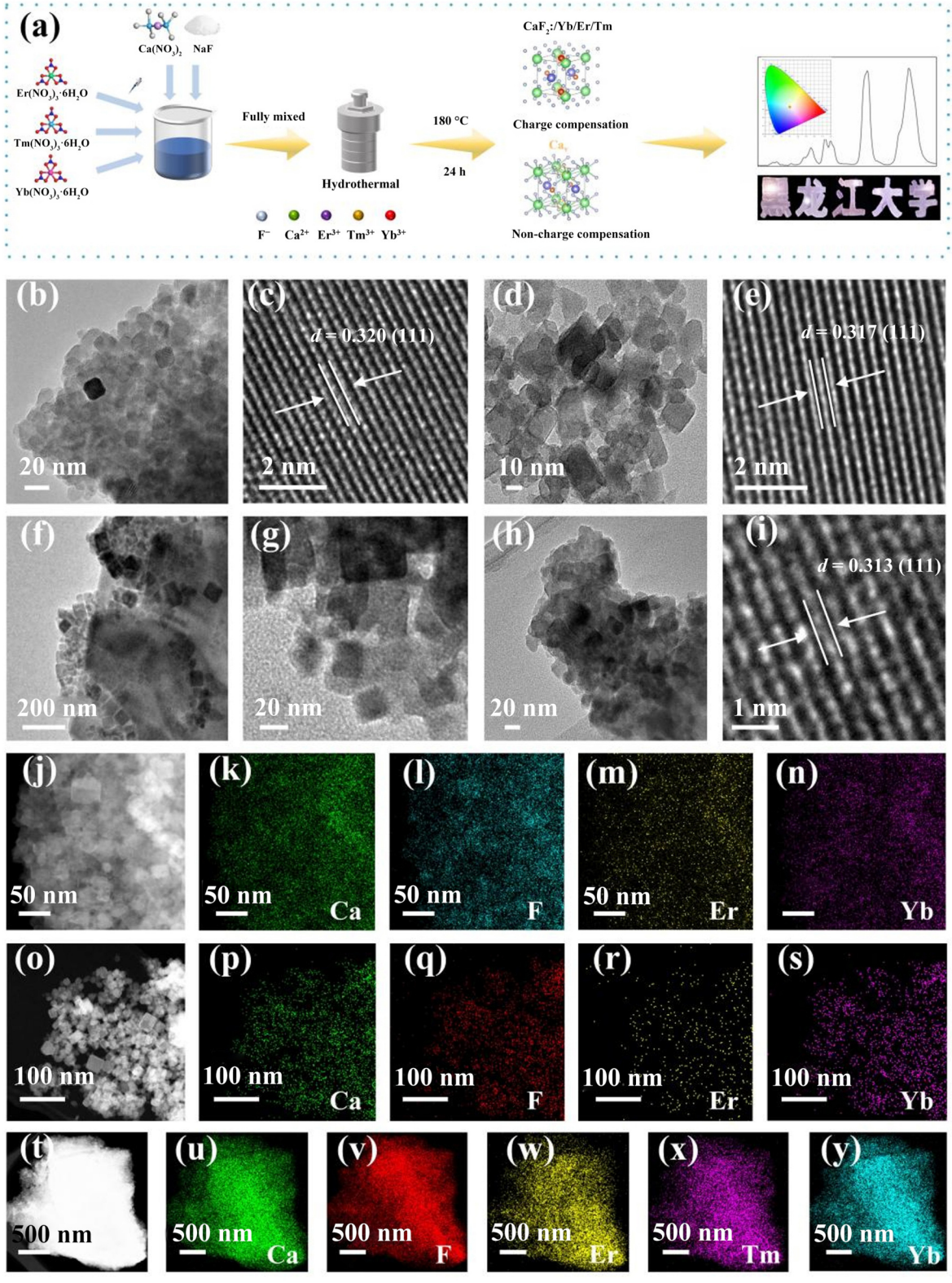

Figure 2 (a) Material synthesis process and charge regulation process. TEM and HRTEM images of (b) and (c) $Ca_{0.78}Yb_{0.2}Er_{0.02}F_2$, (d) and (e) $Ca_{0.67}Yb_{0.2}Er_{0.02}F_2$, (f) and (i) $Ca_{0.697}Yb_{0.2}Er_{0.0015}Tm_{0.0005}F_2$. The element mapping images of Ca, F, Er, and Yb in (j)–(n) $Ca_{0.78}Yb_{0.2}Er_{0.02}F_2$, (o)–(s) $Ca_{0.67}Yb_{0.2}Er_{0.02}F_2$. (t)–(y) The element mapping images of Ca, F, Er, Tm, and Yb in $Ca_{0.697}Yb_{0.2}Er_{0.0015}Tm_{0.0005}F_2$.

0.317 nm in $Ca_{0.67}Yb_{0.2}Er_{0.02}F_2$, indicating a corresponding decrease in lattice vacancies. Energy dispersive X-ray (EDX) spectroscopy results show that the elements F, Ca, Yb, and Er could be detected, demonstrating the successful synthesis of $Ca_{0.697}Yb_{0.2}Er_{0.0015}Tm_{0.0005}F_2$ (Fig. S4 in the ESM). The element mapping results show that F, Ca, Yb and Er are evenly distributed in $Ca_{0.697}Yb_{0.2}Er_{0.0015}Tm_{0.0005}F_2$, which proves that Yb and Er are successfully doped into CaF_2.

In the Fourier transform infrared (FT-IR) spectra (Fig. S6 in the ESM), the bands observed at 2925 and 2855 cm^{-1} are associated with C–H stretching vibrations. The peak at 3429 cm^{-1} is attributed to the stretching vibration of O–H bonds. The peaks at approximately 1564 and 1465 cm^{-1} correspond to the stretching vibrations of C=O and C=C bonds, respectively. Additionally, the peak observed at 723 cm^{-1} is attributed to the stretching vibration of C–F monosubstituted bonds, while the weaker peak at 424 cm^{-1} corresponds to Ca–F.

The ultraviolet–visible (UV–vis) of absorption spectra of CaF_2:Yb^{3+}/Er^{3+} and CaF_2:Yb^{3+}/Tm^{3+} are presented in Fig. S7(a) in the ESM. Charge compensation via RE ion doping leads to a significant enhancement in absorption intensity compared to the samples with non-charge compensation. The UV–vis absorption spectra of CaF_2:Yb^{3+}/Er^{3+} and CaF_2:Yb^{3+}/Tm^{3+} display two absorption peaks at 271 and 283 nm, corresponding to the $\pi \rightarrow \pi^*$ transition of C=C bonds and the $n \rightarrow \pi^*$ transitions of C=O bonds, respectively. For the UV–vis spectrum of the sample with charge compensation in Fig. S7(a) in the ESM there is an absorption peak at 240 nm, indicating a blue shift of the $\pi \rightarrow \pi^*$ transition of the C=C bond. The CaF_2:Yb^{3+}/Er^{3+}/Tm^{3+} samples exhibit absorption peaks at 271 and 283 nm (Fig. S7(b) in the ESM), similar to those of CaF_2:Yb^{3+}/Er^{3+} and CaF_2:Yb^{3+}/Tm^{3+}, but with the absorption intensity significantly enhanced in the visible region above 400 nm. Compared with CaF_2, the absorption intensity of CaF_2:Yb^{3+}/Er^{3+} and CaF_2:Yb^{3+}/Tm^{3+} with charge compensation was increased (Fig. S7 in the EMS) in the ultraviolet region, leading to improved luminescence performance. The bandgap values of CaF_2, $Ca_{0.799}Yb_{0.2}Tm_{0.001}F_2$, $Ca_{0.6985}Yb_{0.2}Tm_{0.001}F_2$, $Ca_{0.78}Yb_{0.2}Er_{0.02}F_2$, and $Ca_{0.67}Yb_{0.2}Er_{0.02}F_2$ were 4.23, 3.83, 3.55, 4.16 and 4.02 eV, respectively. The doping of Tm^{3+} or Er^{3+} can change the bandgap structure of CaF_2, which is consistent with the calculation results above.

The elemental composition and valence states of CaF_2 and CaF_2:Yb^{3+}/Er^{3+} are analyzed using X-ray photoelectron spectroscopy (XPS). The XPS survey spectrum reveals that Ca and F are present in CaF_2, and a small amount of Yb is also present in CaF_2:Yb^{3+}/Er^{3+} (Fig. S8 in the ESM). The high-resolution XPS spectra of CaF_2 and CaF_2:Yb^{3+}/Er^{3+} are shown in Fig. S8 in the ESM. In CaF_2, the high-resolution Ca 2p spectrum (Fig. S8(b) in the ESM) shows the characteristic doublet with peaks at 350.63 ($2p_{1/2}$) and 347.23 eV ($2p_{3/2}$). After Er doping, binding energy shifts are detected for the F 1s, Ca $2p_{3/2}$, and Ca $2p_{1/2}$ peaks, indicating that there is a charge transfer between different elements.

2.3 Optical performance

The UC emission spectra of CaF_2:20%Yb^{3+}/*x*%Er^{3+} (*x* = 0.5, 1, 2, 2.5, and 3) samples and CaF_2:20%Yb^{3+}/*y*%Tm^{3+} (*y* = 0.03, 0.05, 0.1, 0.3, and 0.5) samples are shown in Figs. S11(a) and S11(c) in the ESM, respectively. As shown in Table S1 in the ESM, the effect of different concentrations of Er^{3+} and Tm^{3+} on the luminescence properties of CaF_2 is studied to find the best doping concentration. The luminescence intensity of CaF_2:20%Yb^{3+}/*x*%Er^{3+} increases and then decreases as the Er^{3+} concentration increases from 0.5% to 3%.

The emission intensity reaches its maximum when the concentration of Er^{3+} is 2%. Similarly, in the emission spectrum of CaF_2:20%Yb^{3+}/*y*%Tm^{3+}, the emission intensity is maximized at a concentration of 0.1%Tm^{3+}. The blue emission intensity exhibits a trend of initial increase followed by a decrease with increasing Tm^{3+} concentration: it rises until reaching an optimal level, beyond which concentration quenching causes it to diminish.

The spectral results show that Er^{3+} ions produced efficient green and red UC fluorescence and Tm^{3+} ions produced strong blue UC emission.

The UC emission spectra obtained by exciting Er^{3+} or Tm^{3+} ions with different doping concentrations at 980 nm using a NIR laser show distinct emission features: a strong red emission at 661 nm (Er^{3+}: $^4F_{9/2} \rightarrow {}^4I_{15/2}$), green emissions at 526 and 544 nm (Er^{3+}: $^2H_{11/2}$, $^4S_{3/2} \rightarrow {}^4I1_{5/2}$), and a faint purple emission at 411 nm ($^2H_{9/2} \rightarrow {}^4I_{15/2}$) (Fig. S17 in the ESM). The UC emission spectra for samples with different Tm^{3+} doping concentrations show characteristic blue light emission at 452 and 481 nm, assigned to the $^1D_2 \rightarrow {}^3F_4$, $^1G_4 \rightarrow {}^3H_6$ transitions, respectively, and violet light emission at 346 and 365 nm ($^1I_6 \rightarrow {}^3F_4$, $^1D_2 \rightarrow {}^3H_6$) (Fig. S17 in the ESM). Furthermore, there are also bands observed in the crimson range at 654 and 808 nm originating from the $^1G_4 \rightarrow {}^3F_4$ and $^3F_{2,3} \rightarrow {}^3H_6$ transitions of Tm^{3+}. The generation of UC emission is attributable to the interaction between Yb^{3+}/Er^{3+} and Yb^{3+}/Tm^{3+}.

To further elucidate the mechanism by which charge compensation affects luminescence performance, an in-depth analysis was conducted from the perspectives of crystallography and defect chemistry. In non-charge compensation phosphors, when trivalent Er^{3+}/Yb^{3+} and Tm^{3+}/Yb^{3+} ions partially replace Ca^{2+} in the matrix, the valence mismatch generates excess positive charge, forming cation vacancies (V_{Ca}) to maintain electrical neutrality. The vacancies act as non-radiative recombination centers, which can capture the energy of the excited state and significantly reduce the quantum efficiency of the luminescence. By reducing the Ca^{2+} content effectively modulates the stoichiometric ratio between Ca^{2+} and RE ions in the matrix, thereby decreasing vacancy concentration caused by valence mismatch. The charge compensation method can reduce the vacancy concentration, which can decrease the non-radiation recombination channel, improve the recombination efficiency and increase the luminous intensity.

The UC emission spectra of the CaF_2:20%Yb^{3+}/*x*%Er^{3+} (*x* = 0.5, 1, 2, 2.5, and 3) samples and CaF_2:20%Yb^{3+}/*y*%Tm^{3+} (*y* = 0.03, 0.05, 0.1, 0.3, and 0.5) samples with charge compensation are shown in Figs. S11(b) and S11(d) in the ESM, respectively. CaF_2 with charge compensation is prepared with different molar amounts of Er^{3+} or Tm^{3+} as shown in Table S2 in the ESM. As shown in Figs. 3(a)–3(c), the phosphor with charge compensation exhibits luminescence intensities 1.57, 1.56, and 3.2 times those of its counterpart non-charge compensation, respectively. It is noteworthy that under 980 nm excitation, the characteristic Er^{3+} emissions with charge compensation, namely the strong red peak at 661 nm ($^4F_{9/2} \rightarrow {}^4I_{15/2}$) and the green peaks at 526 and 544 nm ($^2H_{11/2}$, $^4S_{3/2} \rightarrow {}^4I_{15/2}$), are significantly enhanced. By charge compensation, the color of the phosphor also changes, and the corresponding CIE color coordinate of the sample doped with 2% Er^{3+} is shifted from green at point A (0.3299, 0.6303) to yellow at point B (0.4151, 0.5508) (Fig. S15 in the ESM). This shift indicates an increased contribution from red emission, demonstrating that charge compensation effectively enhances the red emission of Er^{3+}.

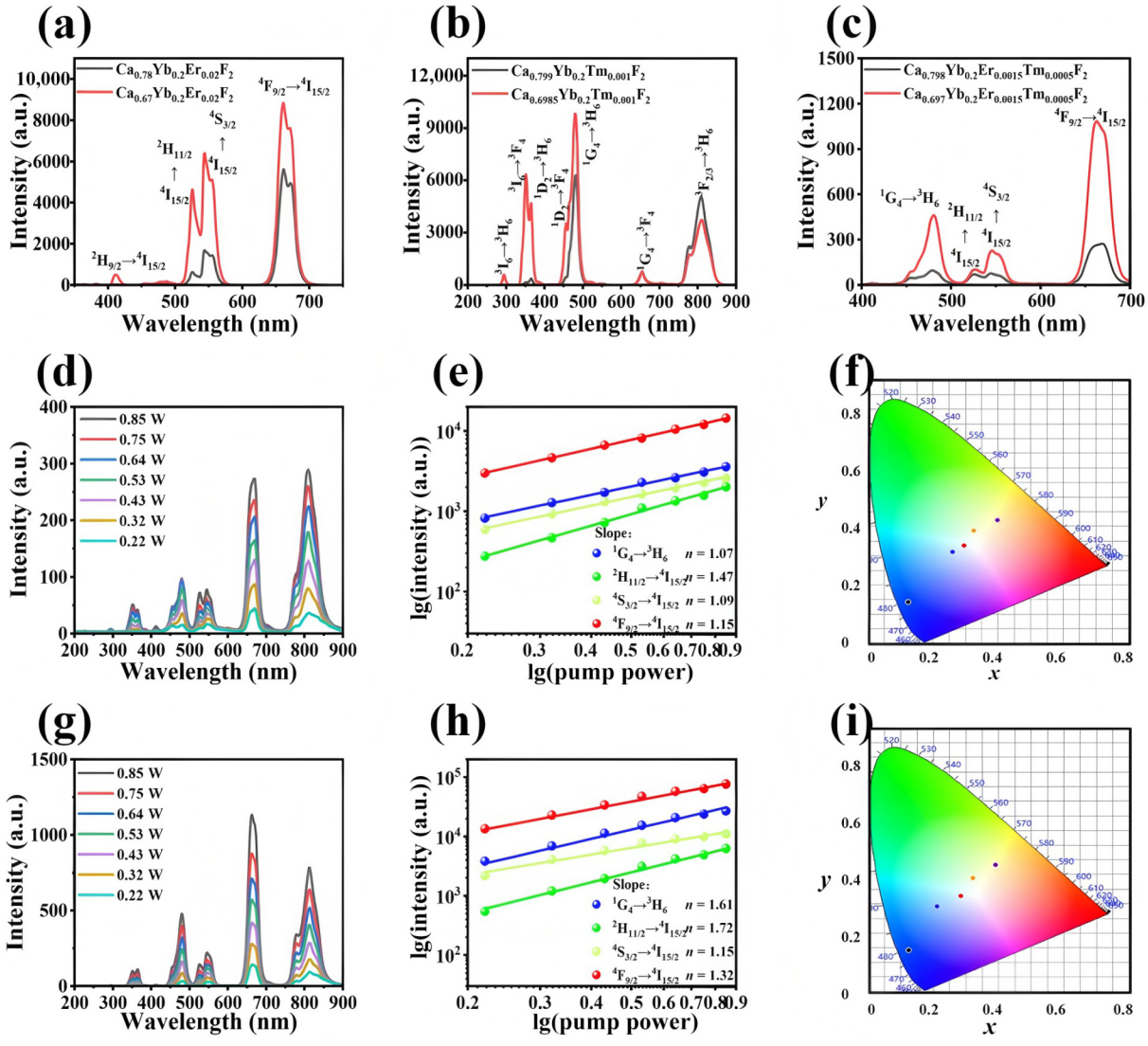

Figure 3 The UC spectra of (a) $Ca_{0.78}Yb_{0.2}Er_{0.02}F_2$ and $Ca_{0.67}Yb_{0.2}Er_{0.02}F_2$, (b) $Ca_{0.799}Yb_{0.2}Tm_{0.001}F_2$ and $Ca_{0.6985}Yb_{0.2}Tm_{0.001}F_2$, and (c) $Ca_{0.798}Yb_{0.2}Er_{0.0015}Tm_{0.0005}F_2$ and $Ca_{0.697}Yb_{0.2}Er_{0.0015}Tm_{0.0005}F_2$. Pump power-dependent UC emission spectra of (d) $Ca_{0.798}Yb_{0.2}Er_{0.0015}Tm_{0.0005}F_2$ and (g) $Ca_{0.697}Yb_{0.2}Er_{0.0015}Tm_{0.0005}F_2$. Double logarithmic plots of pump power versus UC emission intensities of (e) $Ca_{0.798}Yb_{0.2}Er_{0.0015}Tm_{0.0005}F_2$ and (h) $Ca_{0.697}Yb_{0.2}Er_{0.0015}Tm_{0.0005}F_2$. CIE chromaticity diagrams of (f) $Ca_{0.798}Yb_{0.2}Er_{0.0015}Tm_{0.0005}F_2$ and (i) $Ca_{0.697}Yb_{0.2}Er_{0.0015}Tm_{0.0005}F_2$.

In order to investigate the luminescence properties, we adjusted the doping concentrations of Yb^{3+}, Er^{3+}, and Tm^{3+} ions in the CaF_2 host matrix. To investigate the effect of Er^{3+} concentration, the doping levels of Yb^{3+} and Tm^{3+} were fixed at 20% and 0.05%, respectively, in the CaF_2 nanocrystal host. Synthesis was carried out according to the ratios specified in Tables S1 and S3 in the ESM by adjusting the stoichiometry of the CaF_2:Yb^{3+}/Er^{3+}/Tm^{3+}. To accurately represent the true luminescent color, the color coordinates were calculated using the CIE 1931 in Table S3 in the ESM [33]. By varying the Er^{3+} concentration from 0.05 to 0.35%, the color transitions from a blue hue to white and finally to orange-yellow. The chromaticity diagrams depicting the samples with different Er^{3+} concentrations are illustrated in Fig. 3(f). The corresponding CIE coordinates are determined as (0.2114, 0.2909) (0.05%), (0.2341, 0.2781) (0.1%), (0.3018, 0.3299) (0.15%), (0.3221, 0.3860) (0.25%) and (0.3919, 0.4325) (0.35%). As the concentration of Er^{3+} ions increases, the green light emission intensity increases and the blue light emission intensity decreases. In green and red light emissions, Er^{3+} emission decreases due to cross-relaxation between Er^{3+} and Tm^{3+}. From the CIE diagram, it can be observed that the crystal luminescence color achieves a wide range of modulation from blue light, white light to orange-yellow light. When the doping concentration of Er^{3+} ions is 0.15%, the color coordinates (0.3018, 0.3299) of its crystal luminescence are located in the white light region. Its color rendering index is up to 74 (Tables S3 and S11 in the ESM).

A series of CaF_2:Yb^{3+}/Er^{3+}/Tm^{3+} samples with charge compensation, having the nominal formula $Ca_{0.7-1.5x\%}F_2$: 20%Yb^{3+}/x%Er^{3+}/0.05%Tm^{3+} (x = 0.05, 0.1, 0.15, 0.25, and 0.35), were synthesized as detailed in Tables S2 and S4. The Er^{3+} concentration is adjusted from 0.05% to 0.35%, and the color changes from blue to white to green, and the chromaticity diagrams of Er^{3+} samples are shown in Fig. 3(i). The corresponding CIE coordinates are determined as (0.2054, 0.3006) (0.05%), (0.2607, 0.3127) (0.1%), (0.3165, 0.3476) (0.15%), (0.3266, 0.3851) (0.25%) and (0.3998, 0.4211) (0.35%). Through extensive experimental optimization, $Ca_{0.697}Yb_{0.2}Er_{0.0015}Tm_{0.0005}F_2$ sample with charge compensation was obtained. It exhibits CIE coordinates of (0.3165,

0.3476) and a CRI of 84, as shown in Tables S4 and S12 in the ESM.

To better research the power dependence of UC emission intensity, the power-dependent UC luminescence of phosphors with non-charge compensation and with charge compensation was investigated, as shown in Figs. 3(d) and 3(g). The UV emission intensity increased gradually with the increase of the pump power from 119 to 219 mW. The double logarithmic plots of the intensities of blue, green and red UC emissions versus pump power are displayed in Figs. 3(e) and 3(h), and Fig. S13 in the ESM. The fitted power dependence coefficients for the samples with non-charge compensation are 1.47, 1.59, and 1.56 for the 526, 544, and 661 nm emissions, respectively, whereas the corresponding values for the samples with charge compensation are 1.72, 1.15, and 1.32. This indicates that the $^2H_{11/2} \rightarrow {}^4I_{15/2}$, $^4S_{3/2} \rightarrow {}^4I_{15/2}$, and $^4F_{9/2} \rightarrow {}^4I_{15/2}$ transitions are two-photon processes. To realize blue emission, the $^1G_4 \rightarrow {}^3H_6$ transition at 481 nm requires two-photon absorption. The ultraviolet emission spectra of other samples with pump power dependence, along with the double-logarithmic plots of pump power versus relevant parameters, are shown in Figs. S12 and S13 in the ESM.

2.4 Luminous stability

We performed luminescence stability analysis to investigate the optical properties associated with temperature changes and continuous irradiation time in the near UV [34]. Figures 4(a)–4(h) and Fig. S14 in the ESM show the luminescent emission stability of $Ca_{0.798}Yb_{0.2}Er_{0.0015}Tm_{0.0005}F_2$, $Ca_{0.697}Yb_{0.2}Er_{0.0015}Tm_{0.0005}F_2$, $Ca_{0.78}Yb_{0.2}Er_{0.02}F_2$, $Ca_{0.67}Yb_{0.2}Er_{0.02}F_2$, $Ca_{0.799}Yb_{0.2}Tm_{0.001}F_2$, and $Ca_{0.6985}Yb_{0.2}Tm_{0.001}F_2$ at different temperatures and times. The intensity of the emission peaks decreased slightly with the increase of temperature and time. Moreover, the stability of the phosphor with charge compensation is significantly higher than that of the phosphor with non-charge compensation. The charge compensation effectively reduces the cation vacancy, making the CaF_2 structure stable.

In this study, we dispersed $Ca_{0.798}Yb_{0.2}Er_{0.0015}Tm_{0.0005}F_2$ and $Ca_{0.697}Yb_{0.2}Er_{0.0015}Tm_{0.0005}F_2$ into a highly transparent. The resulting composites were then used to assemble WLEDs devices and fabricate 3D printed models. The thermal stability was improved for the resin-coated $Ca_{0.798}Yb_{0.2}Er_{0.0015}Tm_{0.0005}F_2$ phosphor and $Ca_{0.697}Yb_{0.2}Er_{0.0015}Tm_{0.0005}F_2$ phosphor with charge compensation (Fig. 4(k)). Moreover, the luminescence of the resin-coated $Ca_{0.798}Yb_{0.2}Er_{0.0015}Tm_{0.0005}F_2$ phosphor with non-charge compensation and $Ca_{0.697}Yb_{0.2}Er_{0.0015}Tm_{0.0005}F_2$ phosphor with charge compensation was compared before and after 6 months of placement (Figs. 4(i) and 4(j)). The luminescence intensity did not change significantly after the samples were left for 6 months. The PL intensity of the packaged LED device remained virtually constant over a period of 6 months, demonstrating exceptional long-term stability in air. The inset in Fig. 4(l) shows a photograph of "Heilongjiang University" printed in Chinese characters using the resin-coated sample. Under UV illumination, the $Ca_{0.67}Yb_{0.2}Er_{0.02}F_2$, $Ca_{0.6985}Yb_{0.2}Tm_{0.001}F_2$, and $Ca_{0.697}Yb_{0.2}Er_{0.0015}Tm_{0.0005}F_2$ emit blue, green, and white light, respectively, maintaining their original luminescent characteristic. The uniform distribution of luminescence across the printed models indicates the excellent

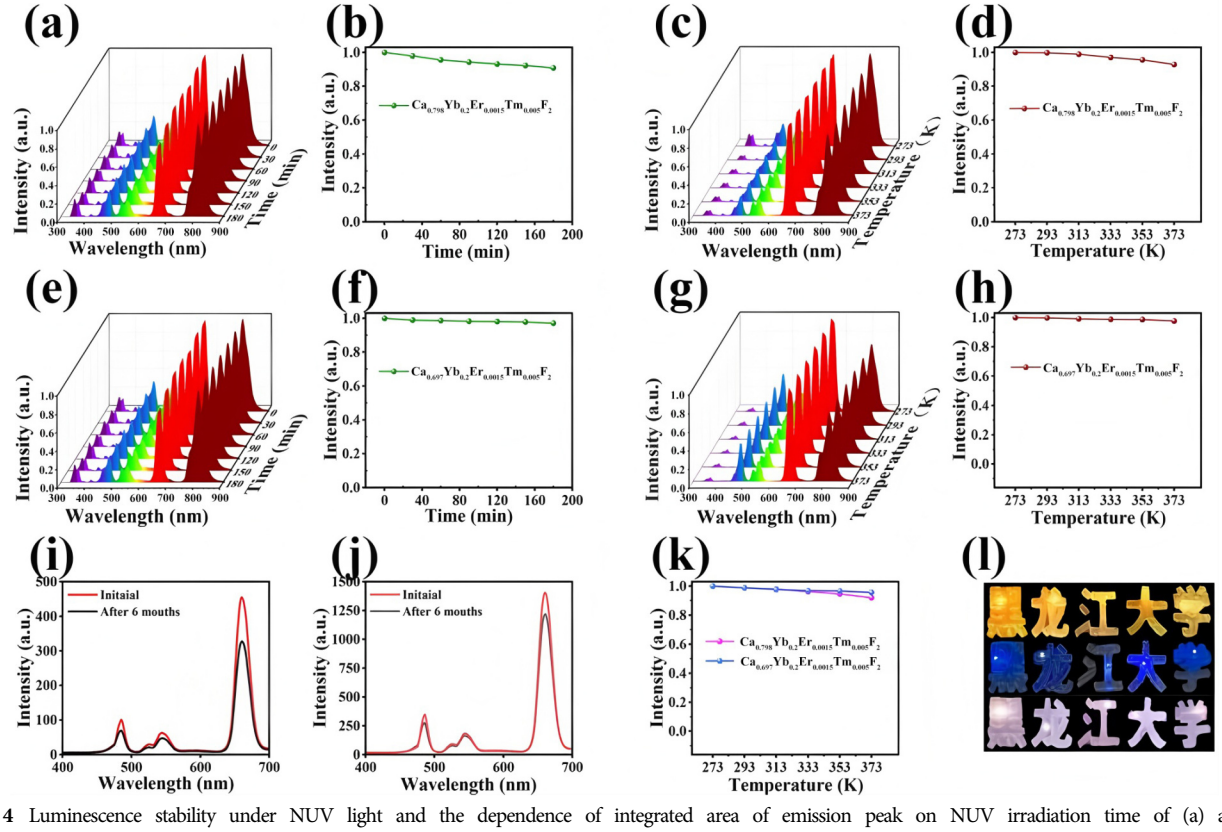

Figure 4 Luminescence stability under NUV light and the dependence of integrated area of emission peak on NUV irradiation time of (a) and (b) $Ca_{0.798}Yb_{0.2}Er_{0.0015}Tm_{0.0005}F_2$ and (e) and (f) $Ca_{0.697}Yb_{0.2}Er_{0.0015}Tm_{0.0005}F_2$. Temperature-dependent emission spectra and the corresponding fluorescence intensity changes of (c) and (d) $Ca_{0.798}Yb_{0.2}Er_{0.0015}Tm_{0.0005}F_2$ and (g) and (h) $Ca_{0.697}Yb_{0.2}Er_{0.0015}Tm_{0.0005}F_2$. Comparison of the UC white luminescence before and after 6 months of storage: (i) $Ca_{0.798}Yb_{0.2}Er_{0.0015}Tm_{0.0005}F_2$ and (j) $Ca_{0.697}Yb_{0.2}Er_{0.0015}Tm_{0.0005}F_2$. UC luminescence stability of resin coated (k) $Ca_{0.798}Yb_{0.2}Er_{0.0015}Tm_{0.0005}F_2$ and $Ca_{0.697}Yb_{0.2}Er_{0.0015}Tm_{0.0005}F_2$. (l) The illustration is the photograph of printings of the Chinese character "Heilongjiang University".

dispersibility and stability of the phosphors in the resin matrix.

2.5 Applications in WLEDs

In this study, we further explored the application of these materials in WLEDs, and constructed WLEDs by depositing $Ca_{0.798}Yb_{0.2}Er_{0.0015}Tm_{0.0005}F_2$ materials onto the surface of 940 nm chips. As described above, the CCT of the WLEDs can be tuned through two approaches: by varying the operating voltage of the devices and by adjusting the $Ca_{0.798}Yb_{0.2}Er_{0.0015}Tm_{0.0005}F_2$ ratios. Tables S5 and S6 in the ESM present the color coordinates corresponding to WLEDs devices under different voltage conditions. When the voltage is 3.4 V, the corresponding color coordinates are (0.3646, 0.3647) and the CCT is 4384 K. When the voltage is 3.5 V, the corresponding color coordinates are (0.3557, 0.3568) and the CCT is 4635 K. When the voltage is 3.6 V, the corresponding color coordinates are (0.3481, 0.3553) and the CCT is 4902 K. Among these, the color coordinates at 3.6V are closest to white light. Table S7 and Fig. S9 in the ESM display the CIE coordinates, CRI, CCT, gamutindex (R_g) and radiative luminous efficiency (LER) values for various WLEDs. The CIE coordinates of the five WLEDs (1–5) are (0.3086, 0.3366), (0.3481, 0.3553), (0.3836, 0.3671), (0.3956, 0.4022) and (0.4074, 0.3806), respectively (Figs. 5(a) and 5(b)). The chromaticity diagram indicates the CCT of the WLEDs in the CIE 1976, confirming that a broad range of white light emission can be achieved. The obtained spectral CRIs of the WLEDs are 78, 75, 79, 83, and 81, respectively, and the corresponding CCTs are 6659, 4902, 3837, 3806, and 3368 K, respectively, demonstrating how different phosphor ratios influence spectral distribution and CCT values. These phosphor compositions produce WLEDs exhibiting high color fidelity and a broad color gamut (high R_g). Furthermore, the WLEDs feature CRIs of 75–83 and a CCT range of 3368–6659 K, delivering both outstanding color quality and a suitable CCT range. The obtained LED-2 color coordinates are (0.3481, 0.3553) near the CIE standard white point, with a CRI of 75 and a CCT of 4902 K. Furthermore, the device exhibits a very small Duv of 0.0007 and an LER of 106 lm/W.

To investigate the effect of charge compensation on the luminescent properties of WLEDs, devices were fabricated by packaging the phosphors with the highest emission intensity onto 940 nm LED chips. The values of CIE coordinates, CRI, CCT, and LER for different WLEDs constructed with the $Ca_{0.697}Yb_{0.2}Er_{0.0015}Tm_{0.0005}F_2$ phosphor with charge compensation are shown in Table S8 in the ESM. The CIE coordinates of the five WLEDs (1–5) are (0.3394, 0.3640), (0.3686, 0.3662), (0.3738, 0.3720), (0.3926, 0.3787) and (0.4100, 0.3869), respectively (Figs. 5(c) and 5(d)). The obtained spectral CRIs of the WLEDs are 81, 81, 83, 85 and 85, and the corresponding CCTs are 5247, 4270, 4152, 3699, and 3365 K, and R_g are 80, 80, 83, 83, and 84, respectively. The local color fidelity (R_f) across different hue-angle bins, depicted in Fig. S10 in the ESM, indicates uniform color perception. The hue shift and chroma shift analyses confirm minimal spectral deviation. The high gamut representation underscores the LED's ability to accurately reproduce colors, making it suitable for high-fidelity lighting applications. The corresponding CIE color coordinates of the WLEDs are shifted from the point C (0.3481, 0.3553) to the point D (0.3686, 0.3662) by charge compensation (Fig. S15(b) in the ESM). Therefore, charge compensation improves red emission, consistent with the above

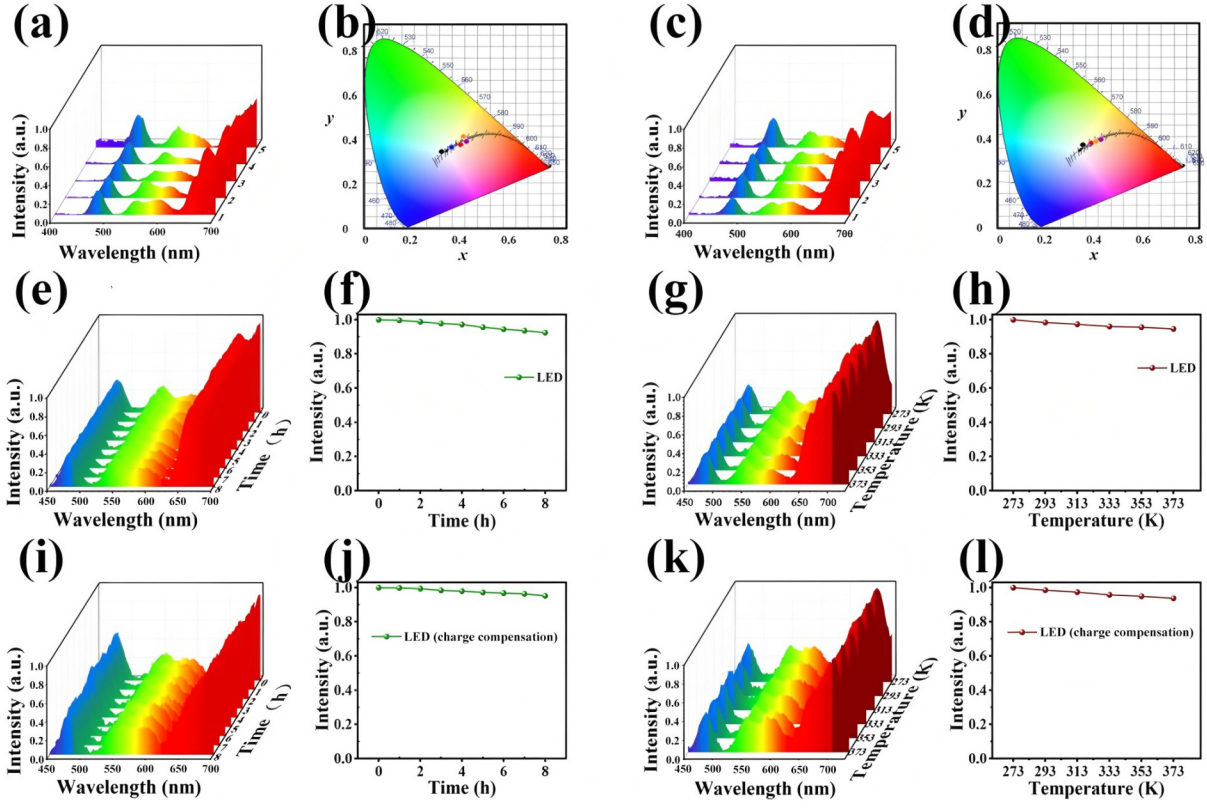

Figure 5 The spectra and corresponding color coordinates of WLEDs devices consisting of (a) and (b) $Ca_{0.798}Yb_{0.2}Er_{0.0015}Tm_{0.0005}F_2$ and (c) and (d) $Ca_{0.697}Yb_{0.2}Er_{0.0015}Tm_{0.0005}F_2$. The luminescence and corresponding luminescence intensity vary with UV irradiation time and the temperature for (e) and (h) LED-2 device (i)–(l) LED-2 device (charge compensation).

conclusion. The color coordinates of LED-2, fabricated with charge compensation, are (0.3686, 0.3662). This device exhibits a CRI of 81, a CCT of 4270 K, a R_g of 80, and an R9 of 85. In addition, the CRIs of LED-4 and LED-5 are as high as 85, and the deviation value of LED-3 with respect to the Duv of the blackbody emission is less than 0.0002. This indicates that the performance of the WLEDs is excellent.

Stability test results under elevated temperature or constant UV irradiation are presented for WLEDs-2 constructed with $Ca_{0.798}Yb_{0.2}Er_{0.0015}Tm_{0.0005}F_2$ phosphor composites (Figs. 5(e)–5(h)) and for those constructed with charge compensation $Ca_{0.697}Yb_{0.2}Er_{0.0015}Tm_{0.0005}F_2$ phosphor composites (Figs. 5(i)–5(l)). The luminescence intensity remains stable after continuous warming (0–100 °C). Moreover, the luminescence intensity remains virtually unchanged after continuous UV exposure for 8 h. This result underscores the exceptional photostability of both the standard and the WLED-2 devices with charge compensation.

In order to investigate the photovoltaic performance of synthetic phosphors as well as WLEDs for indoor applications, the photovoltaic performance of silicon solar cells is analyzed by irradiating them with blue LED, green LED and WLEDs (Fig. S16 in the ESM). As shown in Tables S9 and S10 in the ESM, the photovoltaic efficiencies of LED-2 and LED-2 with charge compensation are 3.27% and 5.90%, when the operating voltage is 3.2 V (Figs. S16(a) and S16(d) in the ESM). The photocurrent intensity increases with increasing operating voltage, and the output photocurrent is highly stable. Figure S16 in the ESM illustrates the transient photocurrent of the solar cell under illumination by a blue LED, a green LED, and the fabricated WLEDs. The Nyquist curve indicates that the internal resistance of the solar cell increases as the intensity of LED illumination increases.

3 Conclusions

In summary, we have successfully synthesized a series of CaF_2:Yb^{3+}/Er^{3+}/Tm^{3+} UC phosphors via a hydrothermal method and systematically demonstrated that a synergistic strategy combining charge compensation and 3D printed resin encapsulation can profoundly enhance both luminescence performance and long-term stability. The structures of CaF_2 and CaF_2:Yb^{3+}/Tm^{3+} phosphors are optimized using DFT, and their figure of merit, optical properties and charge density difference are calculated. The luminescence results show that the charge compensation has little effect on the structure and microstructure of the phosphors, but it has significantly enhanced the luminescence performance of the phosphors. Compared with the non-charge compensation phosphor, the luminescence intensity of charge compensation samples is significantly enhanced. Among them, the sample with charge compensation is 3.2 times that of the non-charge compensation. To further investigate the luminescence properties, we fabricated CaF_2:Yb^{3+}/Er^{3+}/Tm^{3+} WLEDs with excellent color quality, good visual performance, and ideal CCT. The charge-balanced optimal WLEDs achieve a CRI of 81, with CIE coordinates (0.3686, 0.3662) and a CCT of 4270 K. To improve stability, a layer of light-sensitive resin is applied to the surface of the luminescent material using 3D printing technology. The findings indicate a significant enhancement in the luminescence stability of the resin-coated samples. When exposed to the light emitted by WLEDs, the silicon solar cells are effectively stimulated, resulting in consistent photovoltaic output signals. As a result, CaF_2:Yb^{3+}/Er^{3+}/Tm^{3+} phosphors have a wide range of potential applications in lighting. Despite these promising results, the general applicability of this charge compensation approach to other host matrices beyond CaF_2 remains to be explored, and future work can focus on further optimizing 3D printing parameters, such as resin layer thickness and transparency, to further improve luminous efficiency and stability.

Electronic Supplementary Material: Supplementary material (experimental section, detailed characterization, spectral optimization, and computational details) is available in the online version of this article https://doi.org/10.26599/NR.2026.94908410.

Data availability

All data needed to support the conclusions in the paper are presented in the manuscript and the Electronic Supplementary Material. Additional data related to this paper may be requested from the corresponding author upon request.

Acknowledgements

This work was supported by the National Natural Science Foundation of China (No. 22271080) and the Joint Guidance Project of Heilongjiang Natural Science Foundation (No. LH2023B020).

Declaration of competing interest

All the contributing authors report no conflict of interests in this work.

Author contribution statement

Y. X. L.: Experiment, data analysis, writing manuscript. G. F. W.: Writing – review & editing, project administration, theoretical calculation, data analysis, funding acquisition. Z. G. B.: Data analysis. A. X.: Manuscript correction. All the authors have approved the final manuscript.

Use of AI statement

None.

References

[1] Ren, Y. D.; Hua, J. B.; Han, Z. X.; Sun, M. S.; Lü, S. C. Brightly luminescent green-emitting halide perovskite light emitting diode by employing the whole single crystal. *Chem. Eng. J.* **2023**, *452*, 139160.

[2] Lu, L.; Guo, Y. Y.; Zhao, B.; Wang, H.; Miao, Y. Q. A new strategy to develop simple and efficient monochrome and white organic light-emitting diodes. *Mater. Today.* **2024**, *74*, 109–120.

[3] Zhang, D. D.; Li, J. S.; Wang, L.; Guo, Y. Q.; Liu, W. P.; Lin, Q. L.; Li, L. S.; Shen, H. B. Nanoshell-driven carrier engineering of large quantum dots enables ultra-stable and efficient LEDs. *Nano Res.* **2024**, *17*, 10453–10459.

[4] Yuan, W. B.; Huang, T. Y.; Zhou, J. P.; Tang, M. C.; Zhang, D. D.; Duan, L. High-efficiency and long-lifetime deep-blue phosphorescent OLEDs using deuterated exciplex-forming host. *Nat. Commun.* **2025**, *16*, 4446.

[5] Zhao, M.; Ge, Y. P.; Li, Y. R.; Song, X. Y.; Xia, Z. G.; Zhang, X. P. Suppressed concentration quenching and tunable photoluminescence in Eu^{2+}-activated $Rb_3Y(PO_4)_2$ phosphors for full-spectrum lighting.

Light Sci. Appl. **2024**, *13*, 266.
[6] Yu, Y. J.; Wang, H. S.; Pan, J. L.; Li, S. N.; Shen, W. S.; Cheng, S. N.; Jin, L. J.; Wang, Y. K.; Li, Y. Y.; Liao, L. S. Monovalent charge compensation enables efficient lanthanide-based near-infrared perovskite LEDs. *Adv. Funct. Mater.* **2023**, *33*, 2305125.
[7] Li, F.; Tu, L. P.; Zhang, Y. Q.; Huang, D. X.; Liu, X. X.; Zhang, X. R.; Du, J. R.; Fan, R. W.; Yang, C. H.; Krämer, K. W. et al. Size-dependent lanthanide energy transfer amplifies upconversion luminescence quantum yields. *Nat. Photon.* **2024**, *18*, 440–449.
[8] Wang, Y. S.; Lou, B. B.; Dang, P. P.; Zhang, G. D.; Wan, Y. J.; Tian, L.; Lian, H. Z.; Hou, Z. Y.; Ma, C. G.; Li, G. G. et al. Enhancement of NIR-II emission of Er^{3+} by doping Fe^{3+} in double perovskites: Multimode luminescence for versatile optoelectronic applications. *Angew. Chem., Int. Ed.* **2025**, *64*, e202416021.
[9] Xu, X. K.; Mo, L. Q.; Li, Y. D.; Pan, X. Q.; Hu, G. Q.; Lei, B. F.; Zhang, X. J.; Zheng, M. T.; Zhuang, J. L.; Liu, Y. L. et al. Construction of carbon dots with color-tunable aggregation-induced emission by nitrogen-induced intramolecular charge transfer. *Adv. Mater.* **2021**, *33*, 2104872.
[10] Mehare, M. D.; Mehare, C. M.; Swart, H. C.; Dhoble, S. J. Recent development in color tunable phosphors: A review. *Prog. Mater. Sci.* **2023**, *133*, 101067.
[11] Zhang, Y. Y.; Mao, J.; Zhu, P. F.; Wang, G. F. Tunable multicolor luminescence in vanadates from yttrium to indium with enhanced luminous efficiency and stability for its application in WLEDs and indoor photovoltaics. *Nano Res.* **2023**, *16*, 11486–11494.
[12] Jin, J. C.; Wang, Y. Z.; Han, K.; Xia, Z. G. Rigid phase formation and Sb^{3+} doping of tin (IV) halide hybrids toward photoluminescence enhancement and tuning for anti-counterfeiting and information encryption. *Angew. Chem., Int. Ed.* **2024**, *63*, e202408653.
[13] Li, M. Z.; Sun, Y.; Lu, H. L.; Zhu, P. F.; Wang, R. H.; Wang, G. F. Simultaneous improving luminescence intensity and stability of $CsPbBr_3$: SCN^-@Eu/Zr–Uio-66-NH_2 with tunable emissions from blue to green and applications in indoor photovoltaics. *Nano Res.* **2024**, *17*, 6879–6887.
[14] Liu, X. X.; Tu, L. P.; Li, F.; Huang, D. X.; Ågren, H.; Chen, G. Y. Unravelling size-dependent upconversion luminescence in ytterbium and erbium codoped $NaYF_4$ nanocrystals. *J. Am. Chem. Soc.* **2025**, *147*, 5955–5961.
[15] Zhao, J.; Pan, G. C.; Liu, K. L.; You, W. W.; Jin, S. Y.; Zhu, Y. X.; Gao, H. P.; Zhang, H. F.; Mao, Y. L. Efficient dual-mode emissions of high-concentration erbium ions doped lead-free halide double perovskite single crystals. *J. Alloys Compd.* **2022**, *895*, 162601.
[16] Jin, S. L.; Yuan, H.; Pang, T.; Zhang, M. J.; Li, J. Y.; Zheng, Y. H.; Wu, T. M.; Zhang, R. D.; Wang, Z. B.; Chen, D. Q. Highly bright and stable lead-free double perovskite white light-emitting diodes. *Adv. Mater.* **2024**, *36*, 2308487.
[17] Chen, Y. M.; Zhu, H. Y.; Babaian, D.; Dzorkpata, C.; Grigoriev, A.; Wang, Z. W.; Wheat, S.; Guha, S.; Zhu, P. F. Near-unity PLQY of $Cs_3Cu_2X_5$ (X = Cl, Br) for high-efficiency white light-emitting diodes with exceptional color quality. *Adv. Mater.* **2025**, *37*, 2500083.
[18] Fischer, S.; Siefe, C.; Swearer, D. F.; McLellan, C. A.; Alivisatos, A. P.; Dionne, J. A. Bright infrared-to-ultraviolet/visible upconversion in small alkaline earth-based nanoparticles with biocompatible CaF_2 shells. *Angew. Chem., Int. Ed.* **2020**, *59*, 21603–21612.
[19] Geng, H. C.; Peng, R. F.; Wang, J. N.; Dong, Y. T.; Yan, Y. Z.; Dong, J. H.; Xu, L. L.; Kang, H. Y.; Yan, X.; Zhang, X. et al. Synergistic plasmonic and upconversion effect enhanced the photocatalytic activity of the lanthanide-doped CaF_2@TiO_2–Au for antibacterial applications. *Chem. Eng. J.* **2025**, *517*, 164312.
[20] Li, S. G.; Liu, J. Z.; Wu, H. B.; Zhang, X. X.; Guo, Y. Q.; Kang, B. Y.; Zhao, L. M. Up-conversion luminescence and Bi SPR effect promoted Z-scheme $BiVO_4$(040)-Bi-($NaYF_4$:Er,Yb,Tm@BiOBr)/Bi photocatalyst for efficient photocatalytic hydrogen production with simultaneous degradation of malachite green. *Int. J. Hydrogen Energy.* **2024**, *84*, 739–758.
[21] Zernik, W. Theory of infrared optical properties of fluorite crystals. *Rev. Mod. Phys.* **1967**, *39*, 432–439.
[22] Wen, C.; Banshchikov, A. G.; Illarionov, Y. Y.; Frammelsberger, W.; Knobloch, T.; Hui, F.; Sokolov, N. S.; Grasser, T.; Lanza, M. Dielectric properties of ultrathin CaF_2 ionic crystals. *Adv. Mater.* **2020**, *32*, 2002525.
[23] Chauhan, N. S.; Ono, I.; Miyazaki, Y. Lattice anharmonicity in charge compensated higher manganese silicide single crystals. *J. Mater. Chem. A* **2023**, *11*, 19107–19117.
[24] Liu, D. J.; Dang, P. P.; Zhang, G. D.; Lian, H. Z.; Li, G. G.; Lin, J. Near-infrared emitting metal halide materials: Luminescence design and applications. *InfoMat* **2024**, *6*, e12542.
[25] Liu, Y.; Di Stasio, F.; Bi, C. H.; Zhang, J. B.; Xia, Z. G.; Shi, Z. F.; Manna, L. Near-infrared light emitting metal halides: Materials, mechanisms, and applications. *Adv. Mater.* **2024**, *36*, 2312482.
[26] Sun, L. H.; Dong, B.; Sun, J.; Wang, Y. M.; Wang, Y. Q.; Hu, S. T.; Zhou, B. S.; Bai, X.; Xu, L.; Zhou, D. L. et al. Efficient and stable multicolor emissions of the coumarin-modified Cs_3LnCl_6 lead-free perovskite nanocrystals and LED application. *Adv. Mater.* **2024**, *36*, 2310065.
[27] Li, W.; Zhou, D. L.; Fang, Y. H.; Jia, Y. R.; Wang, T. Y.; Wang, Y. Q.; Wang, Y.; Song, R. X.; Wang, E. H.; Bai, X. et al. Energy funnel-driven quantum cutting in Yb^{3+}/Er^{3+}-doped Quasi-2D perovskites enables high-efficiency dual-band near-infrared light-emitting diodes. *Adv. Funct. Mater.* **2025**, *35*, 2510052.
[28] Liu, G. C.; Xiong, Z.; Chen, W. B.; Zhang, S.; Wang, Y. Z.; Xia, Z. G. $MgAl_2O_4$: Cr^{3+} translucent ceramics with tunable broadband near-infrared luminescence for laser-driven light source detection. *InfoMat* **2025**, *7*, e70020.
[29] Wang, T. Y.; Zhou, D. L.; Wang, Y. Q.; Li, W.; Wang, Y.; Yang, H.; Song, R. X.; Wang, E. H.; Song, R. H.; Fang, Y. H. et al. Lanthanide-based lead-free perovskite materials for visible-range and infrared light-emitting diodes. *Adv. Funct. Mater.* **2025**, *35*, 2504436.
[30] Costa, I. F.; Blois, L.; Paolini, T. B.; Assunção, I. P.; Teotonio, E. E. S.; Felinto, M. C. F. C.; Moura Jr., R. T.; Longo, R. L.; Faustino, W. M.; Carlos, L. D. et al. Luminescence properties of lanthanide tetrakis complexes as molecular light emitters. *Coord. Chem. Rev.* **2024**, *502*, 215590.
[31] Kye, Y. H.; Yu, C. J.; Jong, U. G.; Sin, C. N.; Qin, W. P. Defect properties in Yb^{3+}-doped CaF_2 from first-principles calculations: A route to defect engineering for up- and down-conversion photoluminescence. *J. Mater. Chem. C* **2019**, *7*, 15148–15152.
[32] Niu, Y. P.; Wu, F. G.; Zhuo, Y. F.; Li, J.; Zhang, Q.; Teng, Y.; Xie, X. Z.; Dong, H. F.; Mu, Z. F. Luminescence properties and applications of Ca_2ScTaO_6: Bi^{3+}, Ln^{3+} (Ln = Eu, Sm, Dy, Tb) phosphors. *Ceram. Int.* **2025**, *51*, 30597–30603.
[33] Niu, Y. P.; Wu, F. G.; Zhuo, Y. F.; Li, J.; Zhang, Q.; Teng, Y.; Xie, X. Z.; Dong, H. F.; Mu, Z. F. Photochromic and long persistent luminescence properties of Bi^{3+} doped $SrGa_4O_7$. *J. Photochem. Photobiol. A: Chem.* **2026**, *472*, 116800.
[34] Zhuo, Y. F.; Niu, Y. P.; Wu, F. G.; Li, J.; Wang, Y.; Zhang, Q.; Teng, Y.; Xie, X. Z.; Dong, H. F.; Mu, Z. F. Super-wide-range tunable emission across NIR-II and NIR-III achieved by B-site cation co-substitution in Ni^{2+}-doped double perovskites for NIR light sources. *J. Mater. Chem. C* **2025**, *13*, 10621–10631.